



Colloidal solution of boron and phosphorus codoped silicon quantum dots—from material development to applications

Fujii, Minoru
Sugimoto, Hiroshi
Kano, Shinya

(Citation)

Japanese Journal of Applied Physics, 61(SA):SA0807

(Issue Date)

2022-01-01

(Resource Type)

journal article

(Version)

Accepted Manuscript

(Rights)

This is the Accepted Manuscript version of an article accepted for publication in Japanese Journal of Applied Physics. IOP Publishing Ltd is not responsible for any errors or omissions in this version of the manuscript or any version derived from it. The Version of Record is available online at <https://doi.org/10.35848/1347-4065/ac1c3f>

(URL)

<https://hdl.handle.net/20.500.14094/90008936>



Colloidal solution of boron and phosphorus codoped silicon quantum dots -from material development to applications

Minoru Fujii^{1*}, Hiroshi Sugimoto^{1,2}, Shinya Kano^{3,4}

¹Department of Electric and Electronic Engineering, Graduate School of Engineering, Kobe University, Rokkodai, Nada, Kobe 657-8501, Japan

²JST-PRESTO, Saitama 332-0012, Japan

³Human Augmented Research Center, National Institute of Advanced Industrial Science and Technology (AIST), Kashiwa, 270-0882, Japan

⁴Sensing System Research Center, National Institute of Advanced Industrial Science and Technology (AIST), Tsukuba 305-8564, Japan

E-mail: fujii@eedept.kobe-u.ac.jp

A core/shell silicon (Si) quantum dot (QD) composed of a crystalline Si core and an amorphous shell, in which boron (B) and phosphorus (P) are very heavily doped, is developed. Because of the amorphous shell, the B and P codoped Si QDs exhibit significantly different physical and chemical properties from undoped ones. The codoped Si QDs are dispersible in polar solvents such as water and alcohol without organic ligands and exhibit stable luminescence in water. Because of the superior properties, the codoped Si QDs have applications in different fields including photonics, biophotonics, photochemistry and electronics. In this article, we discuss the structure and optical and electrical properties of the codoped core/shell Si QDs and show the application potentials in different fields.

1. Introduction

Silicon (Si) quantum dots (QDs) are an attractive alternative to widely used II-VI (cadmium (Cd) chalcogenide) and IV-VI (lead chalcogenide) QDs due to the low toxicity, high biocompatibility, high compatibility to modern microelectronics technology, high photostability, natural abundance, etc.^{1, 2)} In particular, colloidal Si QDs are considered to be a promising material for bio-imaging, -sensing and -medical applications such as targeted cancer therapy.³⁾ Widely used production processes of colloidal Si QDs are a nonthermal plasma synthesis⁴⁾ and high temperature decomposition of hydrogen silsesquioxane (HSQ).⁵⁻⁷⁾ For the past decade, the quality of Si QDs produced by these methods has been improved dramatically. Currently, a clear solution of Si QDs without agglomeration is easily available due to the development of a surface functionalization process.^{5, 6, 8-10)} A very narrow size distribution is achieved by post size purification processes such as density gradient ultracentrifugation¹¹⁾ and size-selective precipitation.⁹⁾ The luminescence energy is controlled in a wide range by the size,^{5, 9)} and the photoluminescence (PL) quantum yield (QY) reaches 60%.^{12, 13)}

Despite these recent progresses, there still remain several issues that should be overcome to make colloidal Si QDs practically useful. For example, the luminescence property of colloidal Si QDs is often very sensitive to the environment and chemical treatment. For example, the luminescence color changes from red to blue by replacing a few atoms terminating the surface.^{10, 14)} Although the surface sensitiveness is sometimes useful, it makes design and production of a composite system for the bio-applications difficult. The low PL stability in oxidizing environment, i.e., in water and in air, is also a problem. The high surface sensitiveness arises from the fact that ligands are directly attached on the surface of a QD; electron and hole wavefunctions penetrate to ligands and thus small modification of the surface molecules significantly affects the property, especially the luminescence property. In II-VI QDs, this problem can be circumvented by the formation of a core/shell structure such as a CdSe/ZnS QD, because wider band gap shell confines an exciton effectively in the core. Unfortunately, Si does not have lattice-matched wider band gap semiconductors and thus the same strategy cannot be applied. An amorphous silica is a possible choice as a shell material. However, formation of a silica shell costs the conductivity of a Si QD and thus the application fields shrink.

Recently, we have succeeded in producing a new type of core/shell Si QDs in the course of research to develop n- and p-type Si QDs.^{15, 16)} The newly developed core/shell Si QD is composed of a crystalline Si core and an amorphous shell, in which boron (B) and

phosphorus (P) are very heavily doped. Different from undoped Si QDs, the core/shell Si QDs can be dispersed in water and alcohol without organic ligands. They exhibit stable luminescence in the visible to near infrared (NIR) range in water and alcohol. Furthermore, in contrast to silica-coated Si QDs, charge carrier transport across the surface is possible in solution and in a QD solid produced from colloidal QDs. These superior properties suggest possible applications of the B and P codoped core/shell Si QDs in different fields including electronics, photonics, biophotonics and photochemistry. In this Progress Review, we summarize recent research on the structure and optical and electrical properties of the B and P codoped core/shell Si QDs over the past several years.

2. Preparation and characterization of core/shell Si QDs

2.1 Preparation

The B and P codoped Si QDs have been produced by two different methods. The first one is solid-state disproportionation of Si-rich borophosphosilicate glass (BPSG) and subsequent chemical etching. The other one is nonthermal plasma synthesis by using H_2 , SiH_4 , PH_3 and B_2H_6 as process gases.¹⁷⁾ In this article, we will focus on codoped Si QDs produced by the former process. The preparation procedure is shown in detail in previous review papers.^{15, 16)} Briefly, an amorphous Si-rich BPSG film is deposited on a substrate by simultaneously sputtering Si, SiO_2 , B_2O_3 and P_2O_5 , and the film is annealed in an inert gas atmosphere to promote the disproportionation into Si nanoparticles (NPs) and a BPSG matrix. The size of Si NPs is controlled by several process parameters such as the annealing temperature and duration and the composition of Si-rich BPSG. For example, by changing the growth temperature from 950°C to 1600°C, the average diameter changes from 1 nm to over 200 nm.¹⁸⁾ Since quantum size effects become prominent below ~10 nm in diameter in Si crystal, in this article, we will focus on the size range smaller than ~10 nm. After annealing, BPSG matrices are etched out in hydrofluoric (HF) acid solution, and liberated Si QDs are transferred to methanol. It is noted here that sputtering is not a necessary process for the preparation of Si-rich BPSG and thus the formation of core/shell Si QDs. It can also be produced by a vacuum free process.¹⁹⁾

Although we focus on B and P codoped Si QDs in this Progress Review, there have been much more theoretical and experimental researches on either B or P singly-doped Si QDs²⁰⁻²⁴⁾ for optoelectronic device applications. The p- or n-type doped Si QDs usually have a low luminescence QY due to the Auger process,²⁵⁾ and thus not suitable for light emitting applications. On the other hand, in an ideal codoped Si QD, in which carriers are perfectly

compensated, a high luminescence quantum yield is expected. However, doping exactly the same number of B and P to each Si QD is apparently impossible, and thus many of QDs in a sample are not perfectly compensated. In fact, the codoped Si QDs discussed in this paper is usually slightly p-type when the size is relatively large ($> \sim 3.5\text{nm}$).^{26, 27)} This may be one of the reasons to limit the luminescence QY of relatively large QDs. We will discuss it in 2.4. It should be stressed here that the chemical and physical properties of codoped Si QDs are significantly different from singly B-doped p-type Si QDs even if the carrier concentration is similar. Many of the properties discussed in this article is obtained only for codoped Si QDs.

2.2 Structural characterization

Figure 1a shows TEM images of codoped Si NPs grown by annealing Si-rich BPSG at 1200°C for 60-1800 s.²⁸⁾ For the TEM observations, methanol solutions of Si NPs were dropped on an atomically thin graphene oxide support film and dried. After 60 s annealing, the NPs are predominantly amorphous and a very tiny crystalline Si core is observed in an amorphous NP. As the annealing duration increases, the crystalline core grows and the amorphous region shrinks. After 1800 s annealing, a clear core/shell structure is formed. The lattice fringes correspond to the {111} planes of crystalline Si. FTIR, XPS and Raman scattering spectra²⁹⁾ in combination with atom probe tomography (APT)^{30, 31)} reveal that the amorphous shell is composed of Si, B and P; the B and P concentration is higher than their solid solubility limits in bulk Si crystal. This suggests that during the growth of a crystalline Si core by annealing Si-rich BPSG, excess B and P atoms are expelled to the surface to keep their concentration in a crystalline core below the solid solubility limits. In fact, the thickness of the amorphous shell increases as B and P concentrations in Si-rich BPSG increase; the shell thickness reaches $\sim 1.4\text{ nm}$ when B and P concentrations are very high.²⁹⁾ If we further increase the B and P concentrations, Si QDs are no longer formed and cubic BP nanocrystals (NCs)^{32, 33)} and mixture crystals of Si and BP NCs³⁴⁾ are formed by the same procedure. These are interesting nanomaterials having possible applications as photocatalysts,^{33, 35, 36)} but are not a subject of this article.

The amorphous shell in B and P codoped Si QDs induces negative potential on the surface,^{37, 38)} which makes the QDs dispersible in polar solvents by electrostatic repulsions. The difference between the solutions of codoped and undoped Si QDs is clearly visible to the naked eye. Figure 1b shows methanol solutions of undoped and codoped Si QDs prepared by the same procedure.³⁹⁾ The photos just after preparation and after storing for 10 days in

methanol are shown. Just after preparation, the solution of undoped Si QDs is cloudy due to the agglomeration, while that of codoped Si QDs is very clear and the characters behind the vial can clearly be seen. Surprisingly, the color and the transparency do not change for more than 5 years. On the other hand, the brownish opaque solution of undoped Si QDs turns whitish opaque one in 10 days in methanol due to oxidation of Si QDs. Therefore, the amorphous shell in codoped Si QDs not only attains solubility in polar solvents but also brings oxidation resistance, which is important for the applications in photocatalytic H₂ generation and in bio-imaging and -sensing.

The solution dispersibility of codoped Si QDs depends on the doping concentration; it is better in more heavily doped Si QDs.⁴⁰⁾ This is in line with the doping concentration dependence of the shell thickness. It should be stressed here that high solution dispersibility cannot be attained in either B or P singly-doped Si QDs, if they are produced by thermal disproportionation of Si-rich borosilicate glass (BSG) or Si-rich phosphosilicate glass (PSG), respectively. On the other hand, relatively high solution dispersibility is reported in singly B doped Si QDs produced by non-thermal plasma synthesis.^{41, 42)} This suggests that B plays a central role for the high solution dispersibility. The difference between the two preparation methods is the maximum B concentration achievable; higher B doping is expected to be possible by non-thermal plasma synthesis than thermal disproportionation of Si-rich BSG. In fact, in B-doped Si QDs produced by non-thermal plasma synthesis, infrared absorption due to surface plasmon resonances of free holes is observed,²¹⁾ while it is not observed in those produced by thermal disproportionation of Si-rich BSG. In codoped Si QDs, the role of P may be a kind of anchor to hold B in or on the surface of Si QDs and to increase the concentration. In fact, it has been demonstrated by theoretical calculations that formation energy of B and P codoped Si QDs is much smaller than B or P singly doped ones and in codoped QDs, B and P are preferentially doped as a pair.^{24, 43)}

2.3 Size purification

Since Si QDs are dispersed in solution without agglomeration, several size separation processes can be applied to purify the size. The most successful size-purification process is the size-selective precipitation.⁴⁴⁾ In this process, a small amount of poor solvent (toluene) is added to a methanol solution of Si QDs to precipitate Si QDs with the largest size in the size distribution. The precipitate is removed from the solution by centrifugation and is redispersed in methanol. This process is repeated until the supernatant solution becomes colorless. Usually, one solution is separated into 6-10 solutions of Si QDs with

different sizes. A TEM image of size-separated Si QDs is shown in Figure 1c. With this process, the polydispersity of the size distribution, which is defined by a standard deviation (σ) divided by an average diameter (d_{ave}), is reduced to less than 10%. Size separation can also be done by gel electrophoresis.⁴⁵⁾

2.4 Photoluminescence property

In Figure 2a, a luminescence image of a gel after electrophoresis of water solution of codoped Si QDs grown at 1100°C ($d_{ave}=3.5$ nm) is shown together with the PL spectra obtained at different positions of the gel.⁴⁵⁾ Si QDs are size-separated by the gel electrophoresis and a size-dependent shift of the PL is clearly observed. In Figure 2b, the relation between the PL peak energy and the diameter obtained for codoped Si QDs size-separated by a size-selective precipitation process is shown,⁴⁴⁾ together with the data of undoped Si QDs taken from a literature.⁴⁶⁾ The PL energy of codoped Si QDs is much lower than that of undoped Si QDs with the same size. What is remarkable is that the PL peak appears below the band gap energy of bulk Si crystal when the size is relatively large and the B and P concentrations are high. The observation of below-bulk-band-gap PL indicates that the PL arises from in-gap states, most possibly from the donor and the acceptor states. Formation of in-gap states near the conduction and valence band edges was demonstrated in the scanning tunneling spectroscopy (STS).⁴⁷⁾ The size dependence of the energy difference between the two in-gap states in the STS spectra agreed well with that of the PL energy. In Figure 2b, the data obtained from theoretical calculations for Si QDs in which 2, 5 and 10 pairs of B and P atoms are doped are also shown.⁴⁸⁾ Comparison between experiments and calculations suggests that 2-10 pairs of B and P are doped in Si QDs depending on the size and the doping concentration.

Figure 2c shows the relation between the PL QYs and the PL peak energy.⁴⁴⁾ The QY has the maximum around 1.6 eV (~30%) and it decreases at higher and lower energies. Below the bulk Si bandgap, the QYs are less than 1%.^{44, 49)} We studied carrier dynamics of codoped Si QDs by ultrafast spectroscopy.^{50, 51)} The results suggest that the interaction between localized carriers introduced by doping and the photoexcited electron-hole pairs depends on the size, and the relatively efficient interaction in large QDs quenches the PL. It should be stressed here that, although the PL QYs of codoped Si QDs are not very high, they exhibit similar values in different environment such as in methanol, in water and in air. This is an important advantage in many applications.

2.5 Self-assembly of Si QDs - formation of secondary structure

A mesoscale particle produced by clustering QDs via weak physical interactions is dubbed a supra-particle. Formation of a supraparticle modifies the property of constituent QDs via coupling of the electronic wave functions or Förster resonant energy transfer (FRET). A supraparticle can also be an optical cavity to confine photons. Furthermore, the structural feature that QDs are localized in a mesoscale space leads to stronger light emission compared to individual QDs, which improves the detection limit of fluorescence bioimaging. The capability to mix different size QDs leads to wide range control of the emission color.

We developed a self-limited self-assembly process to produce supraparticles of Si QDs.⁵²⁾ Figure 3a shows TEM images of Si QDs supraparticles. By adding toluene to a methanol solution of Si QDs, controlled agglomeration of Si QDs occurs and spherical supraparticles around 100 nm in diameter with a narrow size distribution are grown. The structure is stabilized by coating the surface by polyvinylpyrrolidone (PVP) and then by silica. The PL spectra of PVP- and silica-coated Si QDs supraparticles are very similar to those of Si QDs dispersed in solution. Unfortunately, the PL QY of a supraparticle is smaller than that of constituent individual Si QDs due to FRET between Si QDs,^{53, 54)} although the PL intensity of a single supraparticle is still much larger than that of a single Si QD. In addition to highly symmetric supraparticles produced by self-assembly of Si QDs, wires and networks of Si QDs over 1 μm in length can be produced by bridging Si QDs with metal ions (Figure 3b).⁵⁵⁾

2.6 Nanocomposites of Si QDs and plasmonic nanoparticles

It is well-known that localized surface plasmon resonances of metal nanostructures enhance the excitation efficiency and emission rate of a nearby light emitting material. This phenomenon is useful to improve the small absorption cross-section of Si QDs and to enhance the emission rate.⁵⁶⁾ We have developed a composite nanoparticle composed of a gold (Au) nanorod and Si QDs surrounding it.⁵⁷⁾ Figure 3c shows a TEM image of a composite NP producing by attaching Si QDs on a Au nanorod via a spacer.⁵⁸⁾ By the formation of the composite, 7.2-fold enhancement of the luminescence intensity was observed when the distance between Au nanorod surface and Si QDs is 5 nm. The intensity enhancement is mainly due to the Purcell enhancement of the radiative recombination rate of Si QDs.⁵⁸⁾

Si QDs-metal NP composites can also be produced by directly reducing metal salts by Si QDs.⁵⁹⁾ This is a self-limiting growth process similar to the well-known Turkevich method.⁶⁰⁾ For example, by simply mixing a Si QDs solution with a silver nitrate (AgNO_3)

solution, Ag NPs surrounded by Si QDs are produced. This Ag NPs-Si QDs composites show stable antimicrobial activity in water and in air compared to conventional organic-capped Ag NPs.⁶¹⁾

3. Applications of B and P codoped Si QDs

3.1 Luminescence probe to monitor nanoantenna response

The luminescence band of codoped Si QDs is very broad. The full width at half maximum (FWHM) sometimes reaches 400 meV. The large FWHM is partly due to the size distribution. However, even in the single dot PL spectroscopy, the FWHM is larger than 100 meV at room temperature and is distributed in a wide range.⁶²⁾ Broad room temperature PL in single dot spectroscopy has also been reported in undoped Si QDs.⁶³⁾ In undoped Si QDs, the broadening is attributed to the coupling with phonons because the band narrows at low temperature.^{64, 65)} On the other hand, in codoped Si QDs, the PL band is still very broad even at 77 K.⁶²⁾ Although there is a theoretical attempt to explain the mechanism of the broadening by considering electron-phonon coupling,⁶⁶⁾ it is still not fully elucidated.

In many applications of QDs as phosphors, the large FWHM is unfavorable. However, there are several applications which prefer a broad emission source. An example is a fluorescence probe to monitor the performance of nanoantennas that locally enhances the electric fields of incoming light and enhances the radiative rate of an emitter placed nearby (Purcell effect).⁶⁷⁾ We have been studying the performance of many kinds of nanoantennas for the enhancement of light-matter interactions. Figure 4a shows an example of a nanoantenna, which is composed of a Au nanorod and a Au mirror separated by a sub-10 nm scale nanogap.⁶⁸⁾ The structure similar to that in Figure 4 is generally called a nanoparticle on mirror (NPoM) structure and there have been many variations in the shape (nanosphere, nanocube, nanorod, nanowire, etc.) and material (metal and high refractive index dielectric) of a nanoparticle. In these structures, confinement of electromagnetic fields at the nanogap results in the large Purcell factor and strong enhancement of the emission rate of an emitter placed in the gap.^{69, 70)} In order to monitor wavelength dependence of the antenna performance in a wide wavelength range, codoped Si QDs is a very convenient probe because of the broad emission band and the capability to produce a dense monolayer film by a simple wet process.

In the Au nanorod on mirror (NRoM) structure in Figure 4a,⁶⁸⁾ a monolayer of codoped Si QDs 3 nm in diameter is placed in a gap between a Au nanorod and an ultraflat Au film (200 nm in thickness) produced by a template-stripped method.⁷¹⁾ Compared to the

featureless broad PL band of codoped Si QDs on a flat Au film, the PL spectral shape is strongly modified in the NRoM structure and the intensity is significantly enhanced. The PL intensity at the hot spot is estimated to be 900-fold enhanced. By dividing the PL spectrum in a NRoM structure by that on a flat Au film, the PL enhancement factor is obtained (bottom graph). The PL enhancement factor spectrum agrees very well with the scattering spectrum of the NRoM structure. By comparing the spectra with numerical simulations, the modes contributing to the PL enhancement can be identified.

Similar PL enhancement has been observed on a Si NPoM structure in Figure 4b.⁷²⁾ We can see strong enhancement of Si QDs PL in the gap. In this case the Mie resonances of Si NPs instead of localized surface plasmon resonances of metal NPs are the origin of the enhancement. The Si NPoM structure has several advantages compared to NPoM structures using plasmonic NPs. The first one is the broader enhancement band because of the presence of multiple Mie resonance modes. Another advantage is the insensitivity of the resonance wavelength to the gap length. This provides larger tolerance to the variation of the thickness of an emitting material.

3.2 Luminescence probe for bioimaging

Since codoped Si QDs are dispersible in water and exhibit stable PL in water, they are inherently suitable for biophotonic applications. In order to demonstrate the applicability of codoped Si QDs for fluorescence bioimaging, we have cultivated different types of human cells with codoped Si QDs.^{37, 73)} Figure 5a shows a confocal microscope image of human osteoblasts co-cultivated with codoped Si QDs.³⁷⁾ The excitation wavelength is 405 nm. The green emission is the cell autofluorescence and the red one is from Si QDs. The spectra obtained at the designated positions in the image are shown in the right panel. The PL spectrum of Si QDs is almost identical to that in solution. Therefore, codoped Si QDs can be used as a stable fluorescence probe for bioimaging.

We studied the impact of codoped Si QDs (cytotoxicity) to different cell types, i.e., osteoblasts, monocytes, macrophages, and mesenchymal stromal cells, and found that it depends strongly on the cell types, although the mechanism is not clear.⁷³⁾ Furthermore, we found that cultivation conditions significantly affect cellular metabolic activity. For example, absence of a biomolecular protein corona originating from the media supplement on Si QDs leads to a significant decrease in cellular metabolic activity. The results indicate that for bioimaging applications of Si QDs, mechanism of the formation of biomolecular corona,

i.e., Si QDs-protein composites, should be thoroughly studied.

As a simple Si QDs-protein composite system, we studied the interaction between codoped Si QDs and bovine serum albumin (BSA).⁷⁴⁾ We found that a small difference in the size of Si QDs affects the structure of Si QD-BSA composites. When the diameter of Si QDs is ~ 4 nm, a heterodimer (~ 20 nm) composed of one Si QD and one BSA molecule is preferably formed. On the other hand, when the diameter is ~ 7 nm, composites composed of several Si QDs and BSA molecules are formed and the size increases to ~ 50 nm. The Si QD-BSA composites exhibit stable PL in the near-infrared range in phosphate-buffered saline, and thus can be a bio-compatible stable phosphor operating in the NIR range.

One of the advantages of codoped Si QDs as fluorescence probes for bioimaging is the emission wavelength; it covers 700 nm to 1450 nm.³⁸⁾ In the wavelength range, a whole first NIR window (NIR-I) (700-950 nm) and a part of a second NIR window (NIR-II) (1000-1700 nm) of biological tissues are included. Fluorescence imaging in the NIR range has several advantages compared to visible range such as weaker autofluorescence and smaller scattering and absorption cross-sections of bio-substances. In particular, the NIR-I window has been used for bio-imaging due to availability of organic phosphors with high PL QYs. In the NIR-II window, tissue scattering and autofluorescence are further reduced, which makes tissue probing at cm depths with high spatial resolution possible.⁷⁵⁾ Codoped Si can be a promising candidate for fluorescence probes in the NIR-II range if the QY is improved.

In fluorescence bioimaging, autofluorescence of bio-substances degrades the sensitivity. This can be avoided very effectively by using time-gated imaging.⁷⁶⁾ Since luminescence lifetime of bio-substances is of the order of ns and that of Si QDs is ~ 100 μ s due to the indirect nature of the energy band structure, the two signals can be easily separated by time gating and high contrast images are obtained.⁴⁹⁾

3.3 Luminescent probe for biosensing

Organic dyes are the most commonly used fluorescent probes for bio-sensing. However, NIR luminescent organic dyes often suffer from fast degradation and are not suitable for long-term detection. QD phosphors can be a promising alternative because of the inherently high stability. In order to demonstrate the usage of codoped Si QDs for biosensing, we develop a process to conjugate Si QDs and IgG antibodies.⁷⁷⁾ The procedure is shown in Figure 5b. We first functionalize the surface of codoped Si QDs by amino or epoxy groups by using silane-coupling agents,⁷⁸⁾ and then conjugate surface-functionalized Si QDs and IgG antibodies. TEM images in Figure 5b show growth of amorphous objects

20-30 nm in size containing Si QDs. Characterization by electrophoresis and dynamic light scattering (DLS) in combination with TEM observations indicate that multiple Si QDs are bound to an IgG antibody and a few IgG antibodies are bound via the Si QDs. In this work, it is crucial that IgG antibodies maintain the binding property to an antigen after conjugation with Si-QDs. To confirm that we performed a fluorescent immunoassay using influenza virus nucleoprotein as an antigen. Right bottom illustration in Figure 5b shows the schematic of the fluorescence immunoassay for the nucleoprotein detection. By comparing the PL intensity change with that of controls, we confirmed that the binding property of IgG antibodies to antigens is preserved after the process.⁷⁷⁾

3.4 Charge transfer and photocatalytic reaction

One of the characteristic structural features of codoped Si QDs is the open surface. Since the surface is not covered by insulating materials such as organic molecules and silica, atoms, molecules and ions in solution can access to the surface and a variety of charge transfer induced reactions are expected. For example, adding tetrathiafulvalene (TTF), which has the highest occupied molecular orbital (HOMO) near the valence band edge of Si QDs, to the solution of Si QDs increases the PL efficiency, and the effect is larger in smaller Si QDs. (Figure 6a). The size dependence indicates that positively charged defects in Si QDs are compensated by electron transfer from TTF to Si QDs.⁷⁹⁾ This is a kind of chemical doping to Si QDs and suggests the possibility that the carrier density can be controlled by adsorbing molecules.

Similarly, by adding a molecular reductant in water solution of Si QDs, reversible photobrightening, i.e., gradual increase of PL intensity during light irradiation, appears.⁸⁰⁾ Figure 6b (left) shows photos of water solutions of Si QDs under light irradiation, i.e., just after irradiation start (left) and 10 sec after that (right). In distilled water (upper photos), the luminescence becomes weak by irradiation. This is a temporal darkening and the intensity recovers quickly if the solution is in dark. The temporal darkening is considered to be due to trapping of a photoexcited electron to the surface defect and hole accumulation in a QD; a subsequently excited electron-hole pair recombines via the Auger process with the interaction of the accumulated hole. The process is schematically shown in the upper right illustration.

The photodarkening disappears if sodium sulfites (Na_2SO_3) is added as a molecular reductant. As can be seen in the lower left photo, the luminescence becomes bright during the excitation. This could be explained by efficient extraction of accumulated holes by

Na₂SO₃. The process is schematically shown in the lower right illustrations. The results suggest that, because of the open surface, the luminescence property of codoped Si QDs can be reversibly controlled by the surrounding environment.

Because of the high LUMO level, Si QDs act as a photocatalyst to reduce atoms, ions and molecules. We studied size dependence of the photocatalytic activity by monitoring bleaching of rhodamine B (RhB) in a mixture aqueous solution of Si QDs and RhB under light irradiation.⁸¹⁾ We found that the bleaching rate depends on the size and the size dependence can be well explained by the Marcus theory, which considers charge transfer from the LUMO of Si QDs to that of RhB. Codoped Si QDs also work as photocatalysts for hydrogen (H₂) evolution.³⁹⁾ We observed size dependence of the H₂ generation rate similar to the case of RhB bleaching. Analyses of the size dependence revealed that the upper shift of the LUMO level of Si QDs by the quantum confinement effect plays an important role for the photocatalytic reaction.

Since codoped Si QDs are dispersible in alcohol, a high-density flat film is produced simply by drop-coating or spin-coating the solution on a substrate.^{82, 83)} We produced a Si QDs photocathode by drop-coating the solution on an indium tin oxide (ITO) substrate.⁸⁴⁾ In Figure 7a, a photo and a SEM image of a Si QDs film are shown. A dense film with a flat surface is produced by the process. The film is p-type semiconductor. We measured a photoelectrochemical response of a Si QD photoelectrode by the setup shown in Figure 7b. The linear sweep voltammetry under intermittent light irradiation in Figure 7c shows that cathodic photocurrent due probably to proton reduction at the surface is observed (Figure 7d).⁸⁴⁾ The photocathode is relatively stable and cathodic photocurrent is observed for more than 3000 sec under intermittent light irradiation under constant bias. Note that, in undoped Si QDs, only anodic photocurrent due to self-oxidation of Si QDs is observed, and thus they do not work as photocathode for H₂ evolution.

3.5 Electronic and optoelectronic devices

Solutions of codoped Si QDs can be a precursor for the production of flexible electronic devices. In general, to produce a conductive QD film from a solution of organic-capped QDs, a ligand exchange process is required to reduce the height and width of the tunneling barrier. In codoped Si QDs, the process is not necessary because of the ligand-free naked surface. We confirmed that a thin film produced by spin-coating a solution of freshly-prepared hydrogen-terminated Si QDs ($d_{ave}=4$ nm) exhibits semiconducting behaviors without any thermal treatments. The conductivity of the film sandwiched by aluminum and

ITO electrodes (film thickness: 65 nm) (Figure 8a) is $\sim 2 \times 10^{-5}$ S/cm. The film exhibits photocurrent as shown in Figure 8b.²⁷⁾ The conductivity and the photocurrent do not degrade by bending a polyethylene terephthalate substrate in a 5.9-mm bending radius.

Figure 8c shows a drain current versus gate voltage characteristic of a thin film transistor (TFT) produced from hydrogen-terminated codoped Si QDs ($d_{ave}=6.9$ nm). The transistor has a bottom-contact and bottom-gate configuration. A Si QDs film is spin-coated on Au interdigitated electrodes (separation: 20 μ m) on a thermally oxidized Si substrate (SiO₂ thickness: 90 nm). The TFT shows a p-type behavior, which is consistent with the energy-level diagram of codoped Si QDs obtained by photoelectron yield spectroscopy and X-ray photoelectron spectroscopy.²⁶⁾ The hole field-effect mobility μ is 2.2×10^{-7} cm²/V s, which is much smaller than high-mobility compound semiconductor QDs (>10 cm²/V s),⁸⁵⁾ and is a subject of future research.

As shown in Figure 1b, codoped Si QDs have much higher oxidation resistance than undoped Si QDs. However, if we keep them in methanol for a long period, formation of a thin native oxide is inevitable and it affects the electric properties significantly. In fact, a film produced from Si QDs aged for a long period in methanol is almost an insulator due to the tunneling barrier of the native oxide.⁸³⁾ In that case, the charge transport in ambient air is dominated by proton transport through a chain of water molecules adsorbed onto the surface (Figure 8d). In the relative humidity range of 8-83%, the conductivity changes by 5 orders of magnitude (Figure 8e).⁸²⁾ The film can thus be used as a humidity sensor.⁸⁶⁾ The response/recovery time of the sensor to humidity change is 40 ms, which is fast enough to monitor human respiration (Figure 8f). We utilized the fast response to humidity change for a portable sensor to monitor human respiration in real time.^{86, 87)}

When we apply a strong electric field to an insulating film produced from aged Si QD, it exhibits a bipolar resistive switching. Figure 8g shows the results for a film sandwiched by aluminum and ITO electrodes. The resistive switching is attributed to formation and destruction of conductive filaments of oxygen vacancies in surface oxides (Figure 8h).⁸⁸⁾ The resistivity can be controlled gradually by input electric pulses. This suggests the application to synaptic devices.⁸⁹⁾

Codoped Si QDs can be integrated in semiconductor device fabrication processes. For example, codoped Si QDs were embedded in a hafnium oxide (HfO_x) dielectric layer in a metal-insulator-semiconductor (MIS) structure for nonvolatile memory.⁹⁰⁾

4. Conclusions

We discussed the structure and luminescence properties of a newly-developed core/shell Si QD composed of a crystalline Si core and an amorphous shell made from B, Si and P. Because of the amorphous shell, the B and P codoped Si QDs exhibit significantly different physical and chemical properties from undoped ones. The QDs are dispersible in polar solvents such as water and alcohol without organic ligands and have higher oxidation resistance than undoped Si QDs. The QDs exhibit size-dependent PL in a wide wavelength range covering a whole NIR-I and a part of a NIR-II windows of biological tissues. The high stability of the luminescence in aqueous media makes them suitable as phosphors in biophotonics. Furthermore, because of the high oxidation resistance, they work as photocatalysts and photocathodes for H₂ generation. Drawbacks of codoped Si QDs are the low luminescence QY in a long wavelength range and the high resistivity of a film produced from the solution. These are the subject of future studies.

Acknowledgments

This work was partly supported by JSPS KAKENHI Grant Nos. 18K14092, 18KK0141, and 19K22111.

References

- 1) S. Morozova, M. Alikina, A. Vinogradov and M. Pagliaro: *Frontiers in Chemistry*. **8** [191](2020).
- 2) N. Shirahata: *Physical Chemistry Chemical Physics*. **13** [16](2011)7284.
- 3) F. Erogbogbo, K.T. Yong, I. Roy, R. Hu, W.C. Law, W. Zhao, H. Ding, F. Wu, R. Kumar, M.T. Swihart and P.N. Prasad: *ACS nano*. **5** [1](2011)413.
- 4) U.R. Kortshagen, R.M. Sankaran, R.N. Pereira, S.L. Girshick, J.J. Wu and E.S. Aydil: *Chem. Rev.* **116** [18](2016)11061.
- 5) C.M. Hessel, D. Reid, M.G. Panthani, M.R. Rasch, B.W. Goodfellow, J. Wei, H. Fujii, V. Akhavan and B.A. Korgel: *Chem. Mater.* **24** [2](2012)393.
- 6) R.J. Clark, M. Aghajamali, C.M. Gonzalez, L. Hadidi, M.A. Islam, M. Javadi, M.H. Mobarok, T.K. Purkait, C.J.T. Robidillo, R. Sinelnikov, A.N. Thiessen, J. Washington, H. Yu and J.G.C. Veinot: *Chem. Mater.* **29** [1](2017)80.
- 7) S. Terada, Y. Xin and K.-i. Saitow: *Chem. Mater.* **32** [19](2020)8382.
- 8) L. Mangolini and U. Kortshagen: *Adv. Mater.* **19** [18](2007)2513.
- 9) M.L. Mastronardi, F. Maier-Flaig, D. Faulkner, E.J. Henderson, C. Kubel, U. Lemmer and G.A. Ozin: *Nano Lett.* **12** [1](2012)337.
- 10) M. Dasog, G.B. De los Reyes, L.V. Titova, F.A. Hegmann and J.G. Veinot: *ACS nano*. **8** [9](2014)9636.
- 11) M.L. Mastronardi, F. Hennrich, E.J. Henderson, F. Maier-Flaig, C. Blum, J. Reichenbach, U. Lemmer, C. Kübel, D. Wang, M.M. Kappes and G.A. Ozin: *Journal of the American Chemical Society*. **133** [31](2011)11928.
- 12) A. Marinins, R. Zandi Shafagh, W. van der Wijngaart, T. Haraldsson, J. Linnros, J.G.C.

- Veinot, S. Popov and I. Sychugov: *ACS Appl Mater Interfaces*. **9** [36](2017)30267.
- 13) T.A. Pringle, K.I. Hunter, A. Brumberg, K.J. Anderson, J.A. Fagan, S.A. Thomas, R.J. Petersen, M. Sefannaser, Y. Han, S.L. Brown, D.S. Kilin, R.D. Schaller, U.R. Kortshagen, P.R. Boudjouk and E.K. Hobbie: *ACS nano*. **14** [4](2020)3858.
- 14) R. Sinelnikov, M. Dasog, J. Beamish, A. Meldrum and J.G.C. Veinot: *ACS Photonics*. **4** [8](2017)1920.
- 15) M. Fujii, H. Sugimoto and K. Imakita: *Nanotechnology*. **27** [26](2016)262001.
- 16) M. Fujii, H. Sugimoto and S. Kano: *Chem. Commun.* **54** [35](2018)4375.
- 17) R. Limpens, G.F. Pach and N.R. Neale: *Chem. Mater.* **31** [12](2019)4426.
- 18) H. Sugimoto and M. Fujii: *Advanced Optical Materials*. **5** [17](2017)1700332.
- 19) H. Sugimoto, M. Fujii and K. Imakita: *Nanoscale*. **6** [21](2014)12354.
- 20) R. Gresback, N.J. Kramer, Y. Ding, T. Chen, U.R. Kortshagen and T. Nozaki: *ACS nano*. **8** [6](2014)5650.
- 21) H. Zhang, R. Zhang, K.S. Schramke, N.M. Bedford, K. Hunter, U.R. Kortshagen and P. Nordlander: *ACS Photonics*. **4** [4](2017).
- 22) X. Pi, X. Chen and D. Yang: *J. Phys. Chem. C*. **115** [20](2011)9838.
- 23) A.J.J. Almeida, H. Sugimoto, M. Fujii, M.S.S. Brandt, M. Stutzmann and R.N.N. Pereira: *Phys. Rev. B*. **93** [11](2016)1.
- 24) I. Marri, E. Degoli and S. Ossicini: *Prog. Surf. Sci.* **92** [4](2017)375.
- 25) M. Fujii, Y. Yamaguchi, Y. Takase, K. Ninomiya and S. Hayashi: *Appl. Phys. Lett.* **85** [7](2004)1158.
- 26) Y. Hori, S. Kano, H. Sugimoto, K. Imakita and M. Fujii: *Nano Lett.* **16** [4](2016)2615.
- 27) S. Kano, Y. Tada, S. Matsuda and M. Fujii: *ACS Appl. Mater. Interfaces*. **10** [24](2018)20672.
- 28) A. Minami, H. Sugimoto, I.F. Crowe and M. Fujii: *J. Phys. Chem. C*. **122** [36](2018)21069.
- 29) H. Sugimoto, M. Yamamura, M. Sakiyama and M. Fujii: *Nanoscale*. **10** [16](2018)7357.
- 30) K. Nomoto, H. Sugimoto, A. Breen, A.V. Cezguerra, T. Kanno, S.P. Ringer, I.P. Wurfl, G. Conibeer and M. Fujii: *J. Phys. Chem. C*. **120** [31](2016)17845.
- 31) K. Nomoto, H. Sugimoto, X.Y. Cui, A.V. Ceguerra, M. Fujii and S.P. Ringer: *Acta Mater.* **178** (2019)186.
- 32) H. Sugimoto, M. Fujii and K. Imakita: *Rsc Advances*. **5** [11](2015)8427.
- 33) H. Sugimoto, B. Somogyi, T. Nakamura, H. Zhou, Y. Ichihashi, S. Nishiyama, A. Gali and M. Fujii: *J. Phys. Chem. C*. **123** [37](2019)23226.
- 34) K. Nomoto, H. Sugimoto, A.V. Ceguerra, M. Fujii and S.P. Ringer: *Nanoscale*. **12** [13](2020)7256.
- 35) L. Shi, P. Li, W. Zhou, T. Wang, K. Chang, H. Zhang, T. Kako, G. Liu and J. Ye: *Nano Energy*. **28** (2016)158.
- 36) S. Mou, T. Wu, J. Xie, Y. Zhang, L. Ji, H. Huang, T. Wang, Y. Luo, X. Xiong, B. Tang and X. Sun: *Adv Mater.* **31** [36](2019)e1903499.
- 37) L. Ostrovska, A. Broz, A. Fucikova, T. Belinova, H. Sugimoto, T. Kanno, M. Fujii, J. Valenta and M.H. Kalbacova: *Rsc Advances*. **6** [68](2016)63403.
- 38) H. Sugimoto, M. Fujii, K. Imakita, S. Hayashi and K. Akamatsu: *J. Phys. Chem. C*. **117** [22](2013)11850.
- 39) H. Sugimoto, H. Zhou, M. Takada, J. Fushimi and M. Fujii: *Journal of Materials Chemistry A*. **8** [31](2020)15789.
- 40) H. Sugimoto, M. Fujii, K. Imakita, S. Hayashi and K. Akamatsu: *J. Phys. Chem. C*. **116** [33](2012)17969.
- 41) L.M. Wheeler, N.J. Kramer and U.R. Kortshagen: *Nano Lett.* **18** [3](2018)1888.
- 42) S. Zhou, Z. Ni, Y. Ding, M. Sugaya, X. Pi and T. Nozaki: *ACS Photonics*. (2016).
- 43) F. Iori and S. Ossicini: *Physica E*. **41** [6](2009)939.
- 44) H. Sugimoto, M. Yamamura, R. Fujii and M. Fujii: *Nano Lett.* **18** [11](2018)7282.
- 45) M. Fujii, A. Minami and H. Sugimoto: *Nanoscale*. **12** [16](2020)9266.
- 46) Y. Yu, G. Fan, A. Fermi, R. Mazzaro, V. Morandi, P. Ceroni, D.-M. Smilgies and B.A. Korgel: *J. Phys. Chem. C*. **121** [41](2017)23240.

- 47) O. Ashkenazi, D. Azulay, I. Balberg, S. Kano, H. Sugimoto, M. Fujii and O. Millo: *Nanoscale*. **9** [45](2017)17884.
- 48) C. Delerue: *Phys. Rev. B*. **98** [4](2018).
- 49) M. Sakiyama, H. Sugimoto and M. Fujii: *Nanoscale*. **10** [29](2018)13902.
- 50) R. Limpens, H. Sugimoto, N.R. Neale and M. Fujii: *Acs Photonics*. **5** [10](2018)4037.
- 51) R. Limpens, M. Fujii, N.R. Neale and T. Gregorkiewicz: *J. Phys. Chem. C*. **122** [11](2018)6397.
- 52) M. Fujii, R. Fujii, M. Takada and H. Sugimoto: *ACS Applied Nano Materials*. **3** [6](2020)6099.
- 53) K. Furuta, M. Fujii, H. Sugimoto and K. Imakita: *J. Phys. Chem. Lett.* **6** [14](2015)2761.
- 54) H. Sugimoto, K. Furuta and M. Fujii: *J. Phys. Chem. C*. **120** [42](2016)24469.
- 55) Y. Ohata, H. Sugimoto and M. Fujii: *Nanoscale*. **10** [16](2018)7597.
- 56) A. Inoue, H. Sugimoto and M. Fujii: *J. Phys. Chem. C*. **121** [21](2017)11609.
- 57) H. Sugimoto, T. Chen, R. Wang, M. Fujii, B.M. Reinhard and L. Dal Negro: *Acs Photonics*. **2** [9](2015)1298.
- 58) O. Pavelka, S. Dyakov, J. Veselý, A. Fučíková, H. Sugimoto, M. Fujii and J. Valenta: *Nanoscale*. **13** [9](2021)5045.
- 59) H. Sugimoto, M. Fujii and K. Imakita: *Nanoscale*. **8** [21](2016)10956.
- 60) J. Turkevich, P.C. Stevenson and J. Hillier: *Discussions of the Faraday Society*. **11** [0](1951)55.
- 61) A. Inoue, H. Sugimoto and M. Fujii: *Rsc Advances*. **9** [27](2019)15171.
- 62) T. Kanno, H. Sugimoto, A. Fucikova, J. Valenta and M. Fujii: *J. Appl. Phys.* **120** [16](2016)164307.
- 63) J. Valenta, R. Juhasz and J. Linnros: *Appl. Phys. Lett.* **80** [6](2002)1070.
- 64) I. Sychugov, R. Juhasz, J. Valenta and J. Linnros: *Phys. Rev. Lett.* **94** [8](2005)087405.
- 65) I. Sychugov, F. Pevere, J.-W. Luo, A. Zunger and J. Linnros: *Phys. Rev. B*. **93** [16](2016)161413.
- 66) B. Somogyi, E. Bruyer and A. Gali: *The Journal of Chemical Physics*. **149** [15](2018)154702.
- 67) V. Giannini, A.I. Fernández-Domínguez, S.C. Heck and S.A. Maier: *Chem Rev*. **111** [6](2011)3888.
- 68) H. Sugimoto, S. Yashima and M. Fujii: *Acs Photonics*. **5** [8](2018)3421.
- 69) T.B. Hoang, G.M. Akselrod, C. Argyropoulos, J. Huang, D.R. Smith and M.H. Mikkelsen: *Nat Commun*. **6** (2015)7788.
- 70) R. Chikkaraddy, B. de Nijs, F. Benz, S.J. Barrow, O.A. Scherman, E. Rosta, A. Demetriadou, P. Fox, O. Hess and J.J. Baumberg: *Nature*. (2016).
- 71) P. Nagpal, N.C. Lindquist, S.H. Oh and D.J. Norris: *Science*. **325** [5940](2009)594.
- 72) H. Sugimoto and M. Fujii: *Acs Photonics*. **5** [5](2018)1986.
- 73) T. Belinova, L. Vrabcova, I. Machova, A. Fucikova, J. Valenta, H. Sugimoto, M. Fujii and M. Hubalek Kalbacova: *physica status solidi (b)*. **255** [10](2018)1700597.
- 74) A. Inoue, H. Sugimoto, Y. Sugimoto, K. Akamatsu, M. Hubalek Kalbacova, C. Ogino and M. Fujii: *MRS Communications*. **10** [4](2020)680.
- 75) K. Welsher, S.P. Sherlock and H. Dai: *Proc Natl Acad Sci U S A*. **108** [22](2011)8943.
- 76) J. Joo, X. Liu, V.R. Kotamraju, E. Ruoslahti, Y. Nam and M.J. Sailor: *ACS nano*. **9** [6](2015)6233.
- 77) H. Yanagawa, A. Inoue, H. Sugimoto, M. Shioi and M. Fujii: *MRS Communications*. **9** [3](2019)1079.
- 78) T. Kanno, S. Kano, H. Sugimoto, Y. Tada and M. Fujii: *Mrs Communications*. **6** [4](2016)429.
- 79) H. Sugimoto, Y. Hori, Y. Imura and M. Fujii: *J. Phys. Chem. C*. **121** [21](2017)11962.
- 80) K. Inoue, T. Kojima, H. Sugimoto and M. Fujii: *J. Phys. Chem. C*. **123** [2](2019)1512.
- 81) T. Kojima, H. Sugimoto and M. Fujii: *J. Phys. Chem. C*. **122** [3](2018)1874.
- 82) M. Sasaki, S. Kano, H. Sugimoto, K. Imakita and M. Fujii: *J. Phys. Chem. C*. **120** [1](2016)195.

- 83) S. Kano, M. Sasaki and M. Fujii: J. Appl. Phys. **119** [21](2016).
- 84) M. Takada, K. Inoue, H. Sugimoto and M. Fujii: Nanotechnology. (2021).
- 85) C.R. Kagan, E. Lifshitz, E.H. Sargent and D.V. Talapin: Science. **353** [6302](2016).
- 86) S. Kano, K. Kim and M. Fujii: Acs Sensors. **2** [6](2017)828.
- 87) S. Kano, Y. Dobashi and M. Fujii: IEEE Sensors Letters. **2** [1](2018)1.
- 88) T. Kawauchi, S. Kano and M. Fujii: J. Appl. Phys. **124** [8](2018).
- 89) T. Kawauchi, S. Kano and M. Fujii: ACS Appl. Electron. Mater. **1** [12](2019)2664.
- 90) A. Mazurak, R. Mroczynski, J. Jasinski, D. Tanous, B. Majkusiak, S. Kano, H. Sugimoto, M. Fujii and J. Valenta: Microelectron. Eng. **178** (2017)298.

Figure Captions

Fig. 1. (a) TEM images of codoped Si NPs grown by annealing Si-rich BPSG at 1200°C for 60-1800 s.²⁸⁾ Reproduced from ref. ²⁸⁾. Copyright 2018 American Chemical Society. (b) Photographs of undoped and codoped Si QDs in methanol just after (left panels) and 10 days after (right panels) preparation.³⁹⁾ Reproduced from ref. ³⁹⁾. Copyright 2020 Royal Society of Chemistry. (c) TEM image of codoped Si QDs after size separation by size-selective precipitation.⁴⁴⁾ Reproduced from ref. ⁴⁴⁾. Copyright 2018 American Chemical Society.

Fig. 2. (a) PL image of a gel after electrophoresis of water solution of codoped Si QDs grown at 1100°C ($d_{ave}=3.5$ nm), and the PL spectra obtained at different positions of the gel.⁴⁵⁾ Reproduced from ref. ⁴⁵⁾. Copyright 2020 Royal Society of Chemistry. (b) PL peak energies of codoped (high (HBP) and low B and P concentration (LBP) samples) ⁴⁴⁾ and undoped Si QDs (gray squares)⁴⁶⁾ as a function of diameter. Calculated PL energies of Si QDs codoped with different numbers of B–P pairs (2 (∇), 5 (\diamond), and 10 (left pointing triangle) pairs) taken from ref. ⁴⁸⁾ are also shown. Reproduced from ref. ⁴⁴⁾. Copyright 2018 American Chemical Society. (c) Relation between PL QYs and PL peak energy obtained for codoped Si QDs grown at different conditions.⁴⁴⁾ Reproduced from ref. ⁴⁴⁾. Copyright 2018 American Chemical Society.

Fig. 3. (a) TEM images of Si QDs supraparticles produced from codoped Si QDs.⁵²⁾ Reproduced from ref. ⁵²⁾. Copyright 2020 American Chemical Society. (b) TEM image of networks of codoped Si QDs produced by bridging Si QDs with metal ions.⁵⁵⁾ Reproduced from ref. ⁵⁵⁾. Copyright 2018 Royal Society of Chemistry. (c) TEM image of a composite nanoparticle composed of a Au nanorod and Si QDs surrounding it.⁵⁸⁾ Reproduced from ref. ⁵⁸⁾. Copyright 2021 Royal Society of Chemistry.

Fig. 4. (a) Schematic illustration of Au nanorod on mirror structure and a TEM image of a Au nanorod. A monolayer of Si QDs is placed beneath a Au nanorod. (upper graph) PL spectra of a Si QDs monolayer in a nanoantenna and on a Au film. (lower graph) PL enhancement factor spectrum and scattering spectrum of a Au nanorod on mirror structure. Reproduced from ref. ⁶⁸). Copyright 2018 American Chemical Society. (b) Schematic illustration of Si nanosphere on mirror structure. A monolayer of Si QDs is placed beneath a Si nanosphere. (upper graph) PL spectra of a Si QDs monolayer in a nanoantenna and on a Au film. Scattering images in a nanoantenna and on a Au film are also shown. (lower graph) PL enhancement factor spectrum and scattering spectrum of a Si NPoM structure. Reproduced from ref. ⁷²). Copyright 2018 American Chemical Society.

Fig. 5. (a) Wide-field fluorescence microscopy and spectroscopy under cw excitation at 405 nm. (left) combined fluorescence image with the green layer showing the full signal (dominated by cell autofluorescence) and the orange layer showing signal above 785 nm (dominated by Si QD luminescence). (right) Luminescence spectrum of cell autofluorescence (blue) and emission of Si QDs (red line) from area indicated by a rectangle in the left panel. Reproduced from ref. ³⁷). Copyright 2016 Royal Society of Chemistry. (b) Schematic diagram of the procedures of surface functionalization of a Si QD with silane-coupling agents and conjugation of a Si-QD and an IgG antibody. (lower left) TEM images of IgG antibodies and Si QDs composites. (lower right) Schematic illustration of fluorescence immunoassay for anti-influenza A virus nucleoprotein detection.

Fig. 6. (a) HOMO and LUMO levels with respect to the vacuum level of Si QDs with different sizes. The HOMO level of TTF is also shown. PL spectra of Si QDs with different diameters (d_{ave}) (from left to right, d_{ave} = 3.9, 4.5, and 6.5 nm) in mixture solutions with TTF. The numbers in the graphs represent the molar ratio

of TTF to a Si QD (0.5 (dashed curves) and 5 (dotted curves)). Reproduced from ref. ⁷⁹⁾. Copyright 2017 American Chemical Society. (b) (upper left) Photos of water solutions of Si QDs under 405 nm light irradiation (50 mW); (left) just after starting irradiation, (right) after 10 s continuous irradiation. The red stripes are the emission from Si QDs. (lower left) Photos of water solutions of Si QDs containing Na₂SO₃ (100 mM) under 405 nm light irradiation (50 mW); (left) just after starting irradiation, (right) after 10 s continuous irradiation. (right) Schematic illustration of energy diagrams of Si QDs under light irradiation in water with and without molecular reductants. Reproduced from ref. ⁸⁰⁾. Copyright 2019 American Chemical Society.

Fig. 7. (a) Photo and SEM image of a Si QDs film produced from methanol solution of codoped Si QDs. (b) Setup for the measurements of photoelectrochemical property of a Si QDs film. (c) Linear sweep voltammogram of a Si QDs film under intermittent light irradiation. (d) Schematic illustration of energy level diagram. Reproduced from ref.⁸⁴⁾. Copyright 2021 IOP Publishing.

Fig. 8. (a) Schematic of a sample structure for electrical characterization of a hydrogen-terminated Si QDs film. (b) Short-circuit current under 4 kHz-modulated laser irradiation (405 nm, 4.6 mW). (c) Drain current vs. gate voltage characteristics of a TFT produced with hydrogen-terminated codoped Si QDs. Inset is the schematic illustration of a sample structure. Adapted with permission from ref.²⁷⁾. Copyright 2018 American Chemical Society. (d) Proton transport in adsorbed water on the surface of Si QDs with native oxide. (e) Current vs. relative humidity in a film of Si QDs with native oxide ($d_{ave}=6.9$ nm). (f) Monitoring respiratory air by current. Adapted with permission from ref. ⁸⁶⁾. Copyright 2017 American Chemical Society. (g) Bipolar resistive switching behavior of a thin film of Si QDs with native oxide. (h) Schematic illustration of a model for the formation and destruction of conductive filaments by an electric field. HRS: high resistive

state, LRS: low resistive state. Adapted with permission from ref.⁸⁹). Copyright
2019 American Chemical Society.

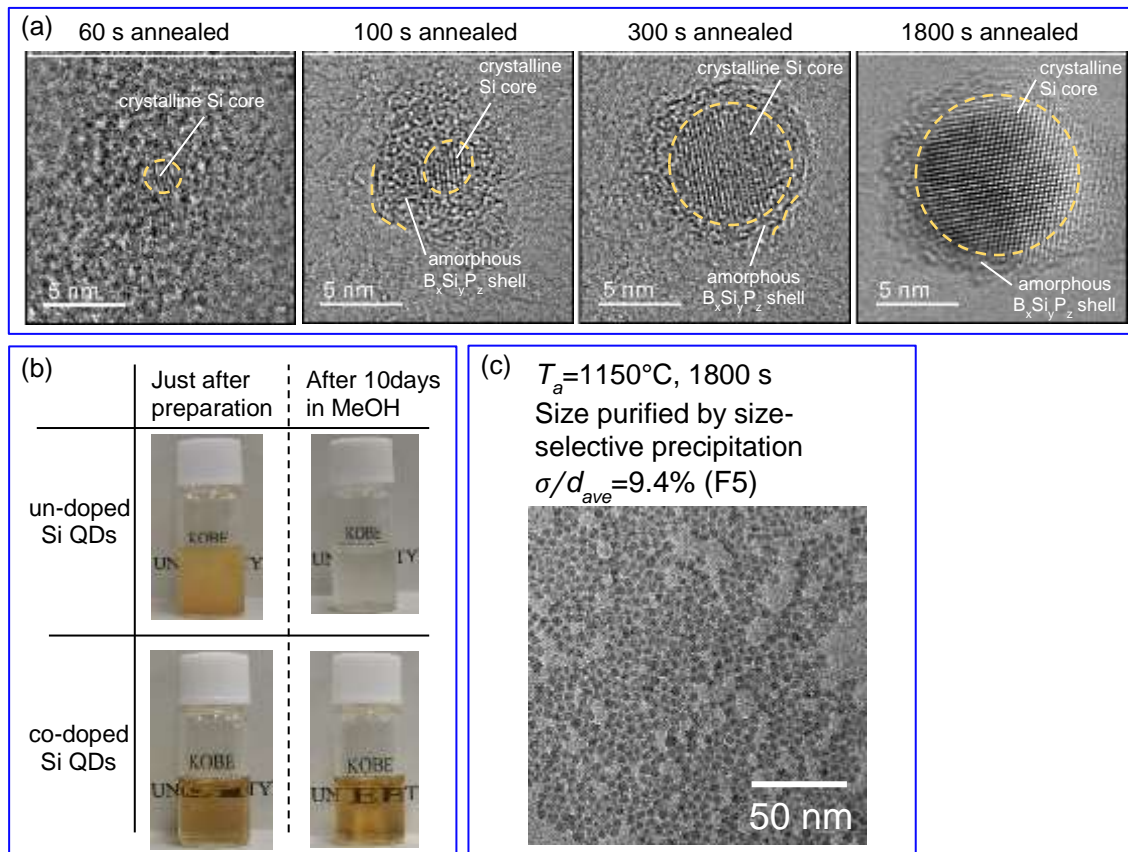


Fig.1.

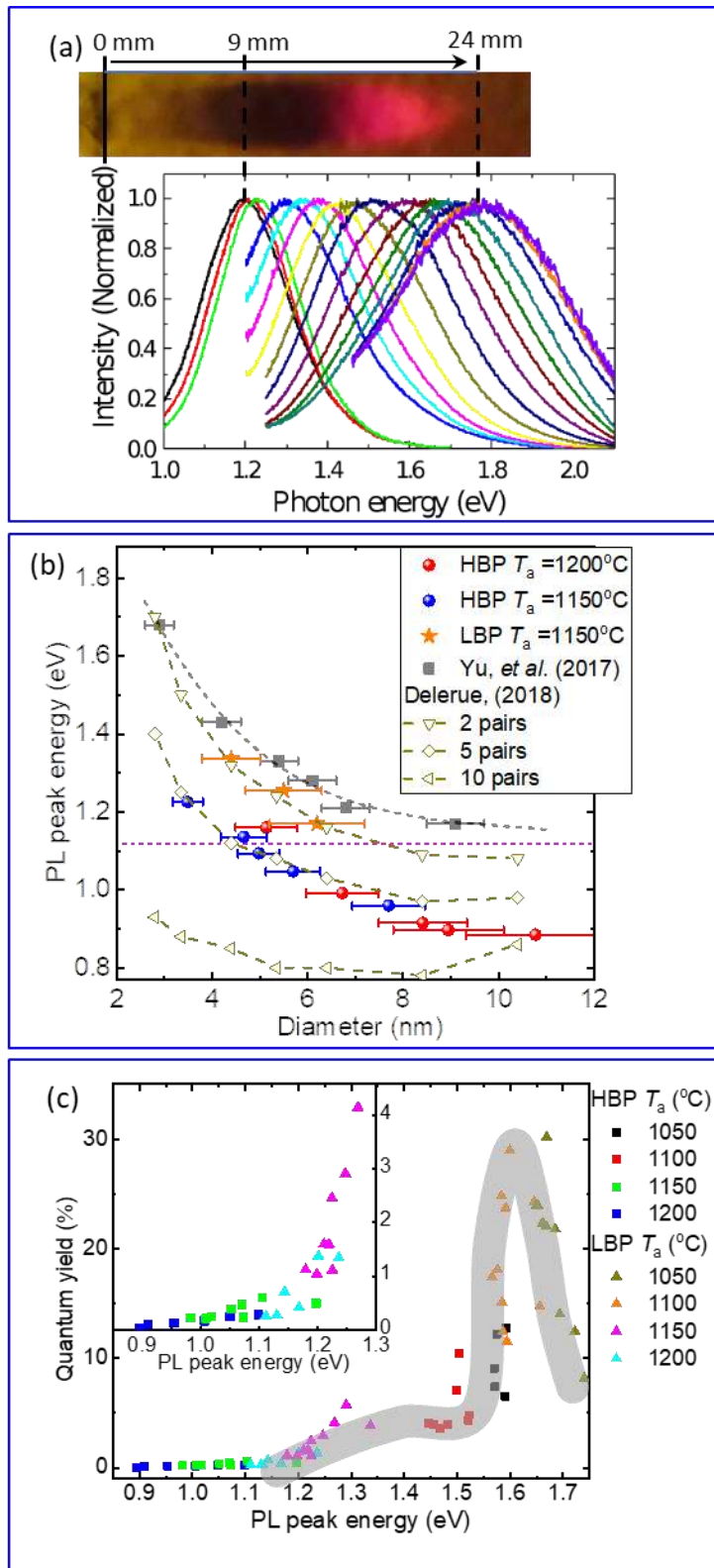


Fig. 2.

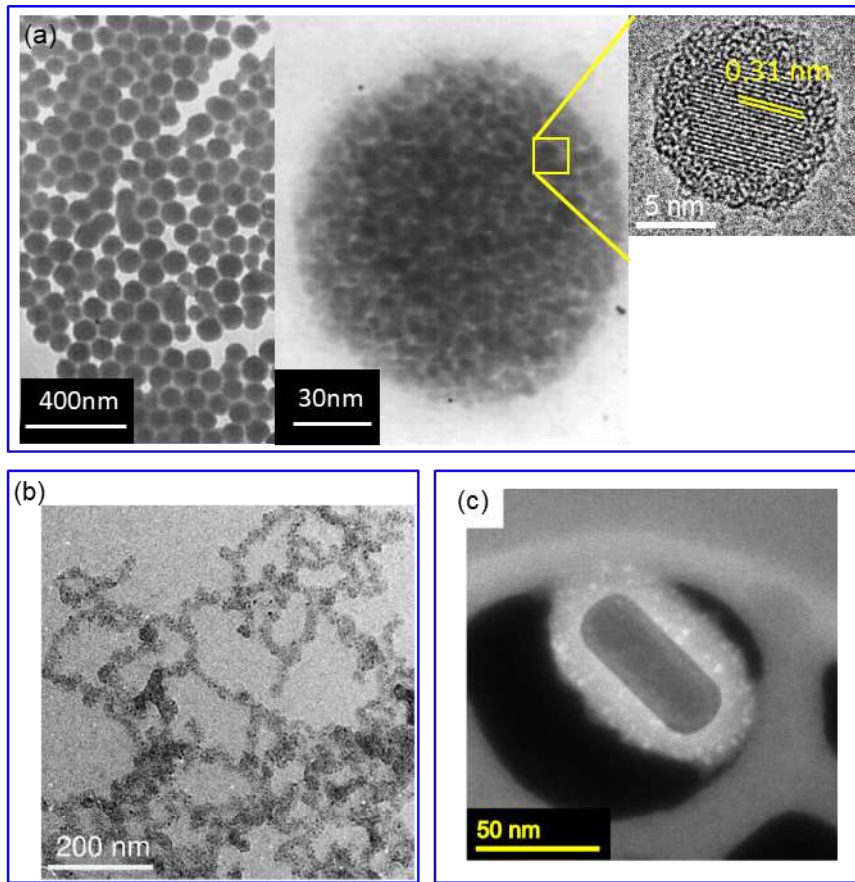


Fig. 3.

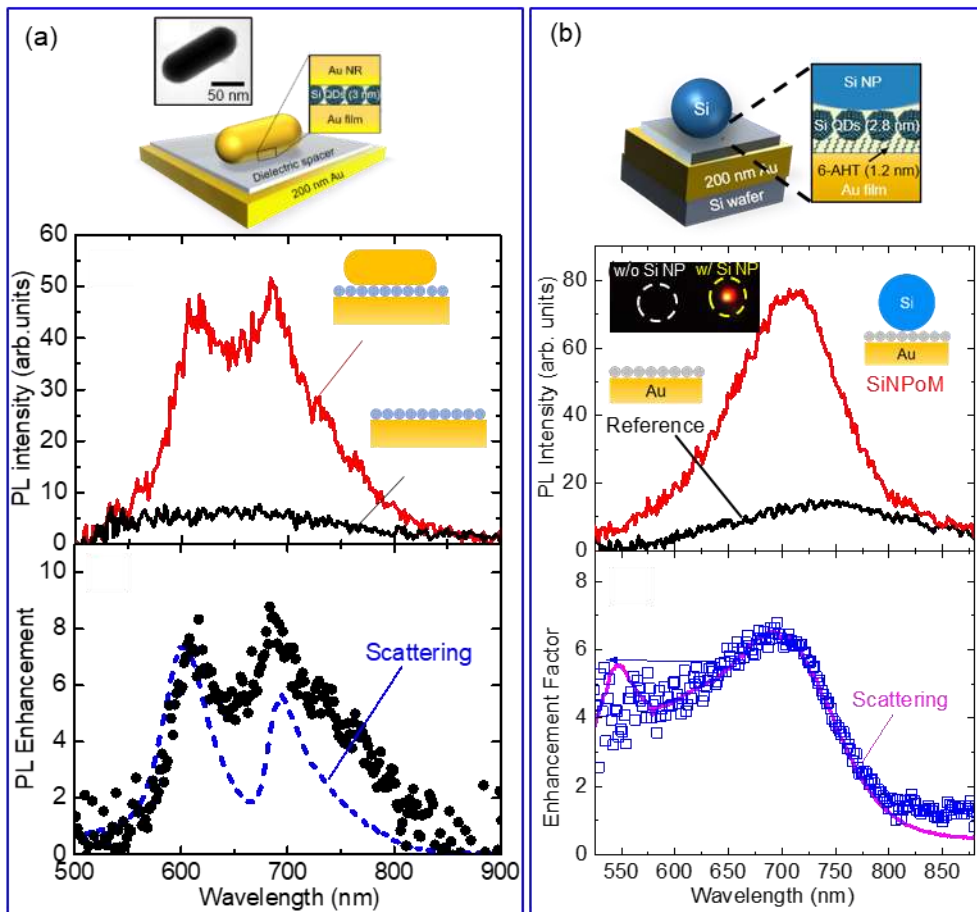


Fig. 4.

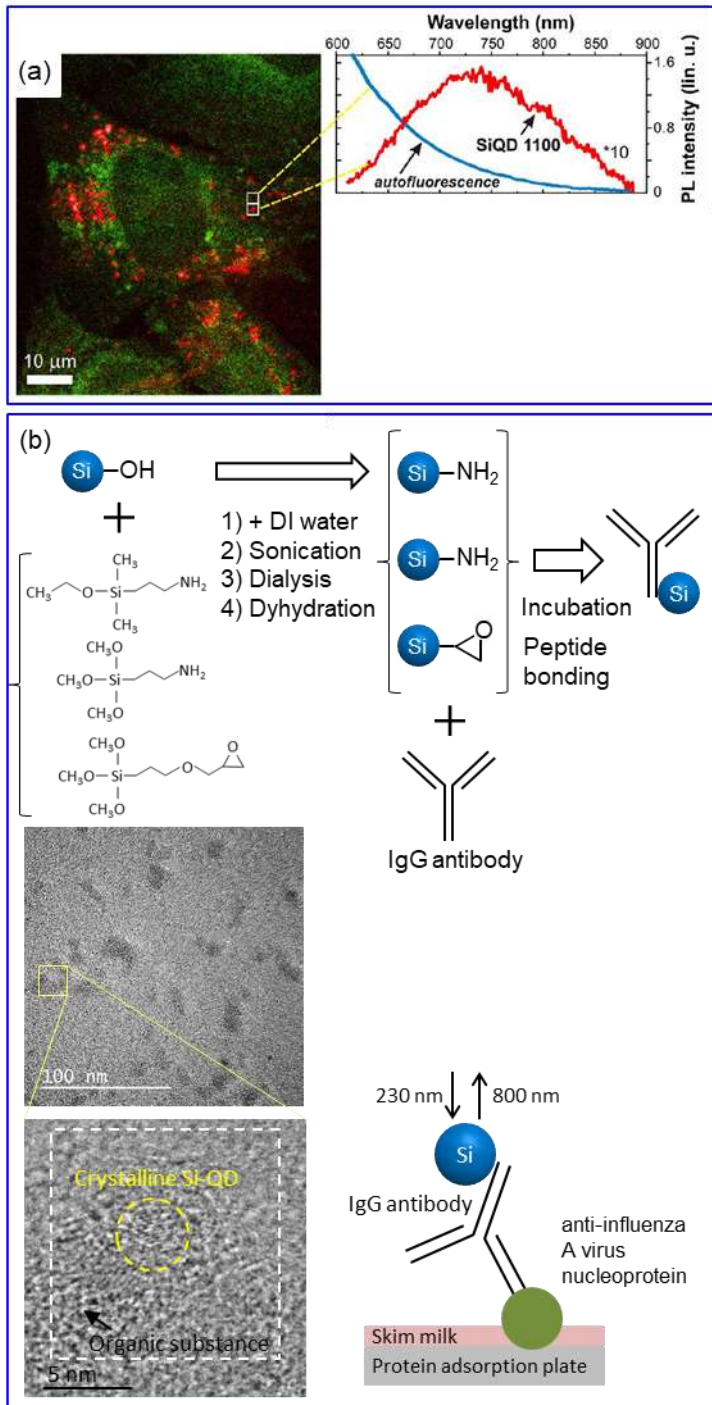


Fig. 5

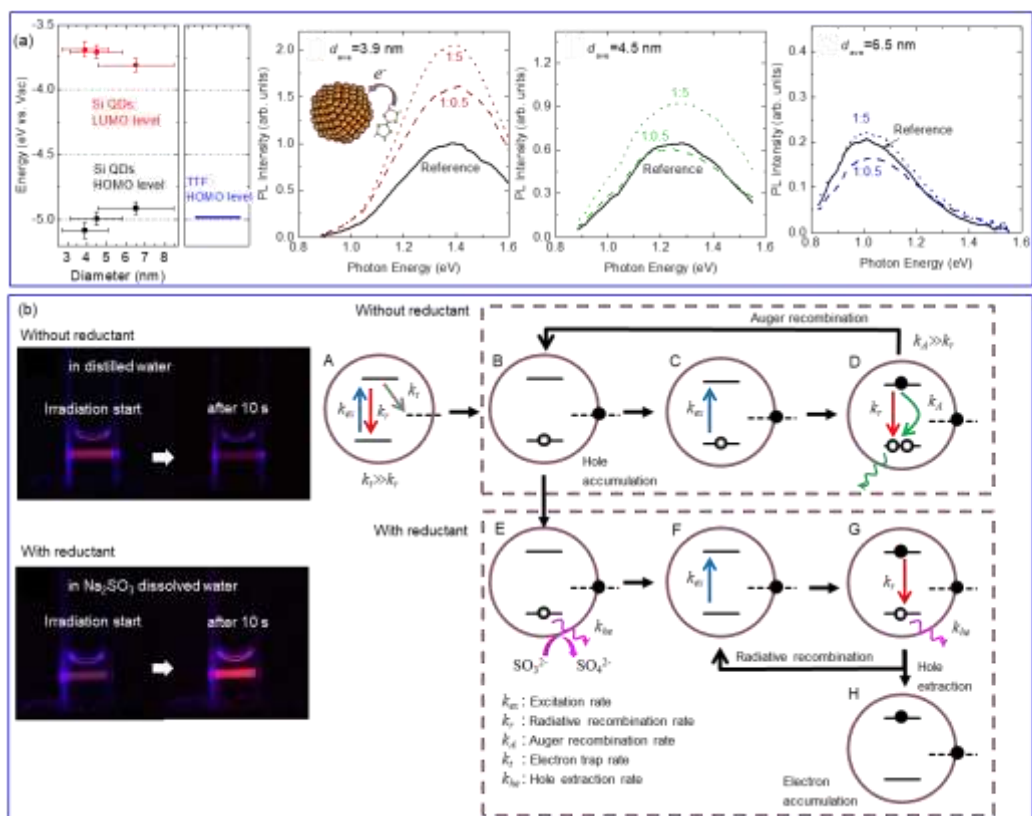


Fig. 6

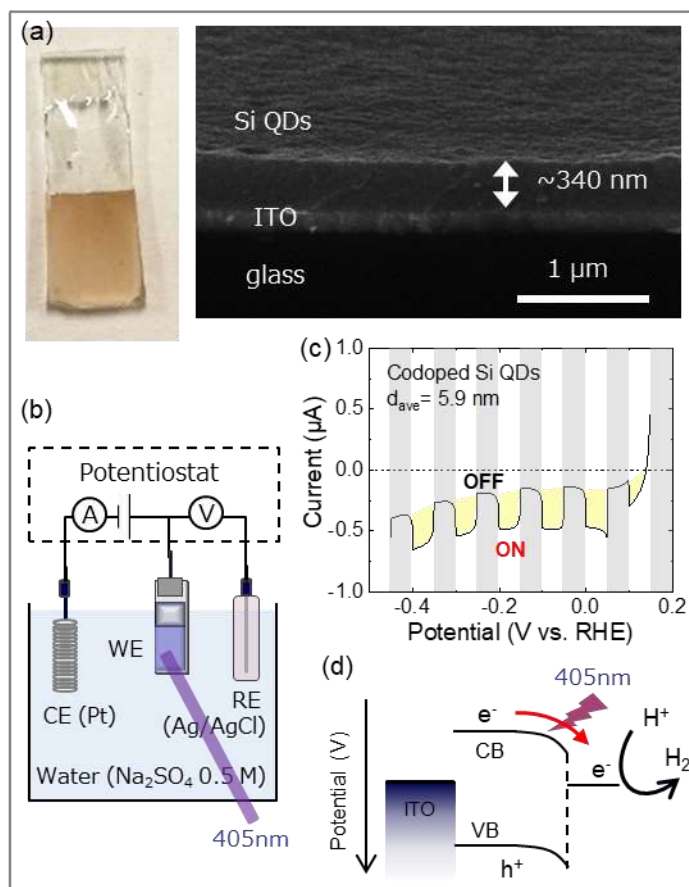


Fig. 7.

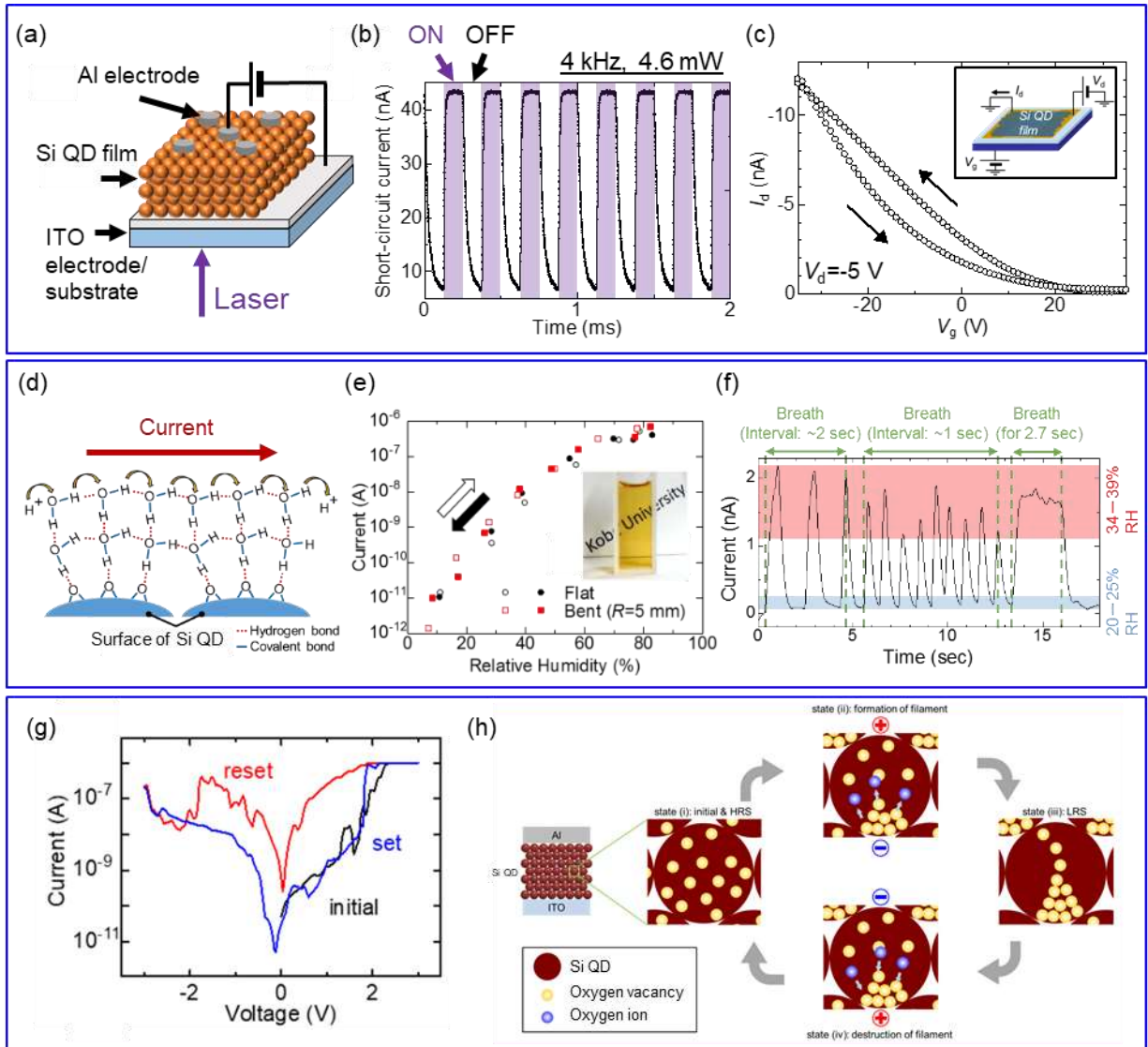


Fig. 8.